



Corundum-structured AlCrNbTi oxide film grown using high-energy early-arriving ion irradiation in high-power impulse magnetron sputtering

Hao Du^{a,b,d,*}, Rui Shu^c, Robert Boyd^b, Arnaud le Febvrier^c, Mauricio A. Sortica^e, Daniel Primetzhofer^{e,f}, Ulf Helmersson^b, Per Eklund^c, Daniel Lundin^{b,*}

^a School of Mechanical Engineering, Guizhou University, Guiyang 550025, PR China

^b Plasma and Coatings Physics Division, Department of Physics, Chemistry, and Biology (IFM), Linköping University, Linköping SE-581 83, Sweden

^c Thin Film Physics Division, Department of Physics, Chemistry, and Biology (IFM), Linköping University, Linköping SE-581 83, Sweden

^d State Key Laboratory of Public Big Data, Guizhou University, Guiyang 550025, PR China

^e The Tandem Laboratory, Uppsala University, Uppsala 75120, Sweden

^f Department of Physics and Astronomy, Uppsala University, Uppsala 75120, Sweden

ARTICLE INFO

Keywords:

High-entropy oxides
HiPIMS
Ion bombardment
Corundum structure
Nanotwin

ABSTRACT

Multicomponent or high-entropy oxide films are of interest due to their remarkable structure and properties. Here, energetic ion irradiation is utilized for controlling the phase formation and structure of AlCrNbTi oxide at growth temperature of 500°C. The ion acceleration is achieved by using a high-power impulse magnetron sputtering (HiPIMS) discharge, accompanied by a 10 μs-long synchronized substrate bias (U_{sync}), to minimize the surface charging effect and accelerate early-arriving ions, mainly Al^+ , O^+ , Ar^{2+} , and Al^{2+} . By increasing the magnitude of U_{sync} from −100 V to −500 V, the film structure changes from amorphous to single-phase corundum, followed by the formation of high-number-density stacking faults (or nanotwins) at $U_{\text{sync}} = -500$ V. This approach paves the way to tailor the high-temperature-phase and defect formation of oxide films at low growth temperature, with prospects for use in protective-coating and dielectric applications.

Multicomponent or ‘high-entropy’ oxides (HEOs) [1] are an emerging subset of the larger class of high-entropy materials [2,3]. As one of the typical HEO families, AlCr-containing high-entropy oxides in either bulk or film form have been synthesized and can exhibit self-repairing properties [4], ferrimagnetism [5], and are of interest for catalysis [6]. Particular interest stems from AlCr-containing high-entropy oxide films grown in a far-from-equilibrium process, e.g., reactive magnetron sputtering. A range of structures has been reported for AlCr-containing high-entropy oxide films, including amorphous [7, 8], rock salt ($\text{Fm}\bar{3}\text{m}$) [9], spinel ($\text{Fd}\bar{3}\text{m}$) [10,11], rutile ($\text{P4}_2/\text{mmn}$) [12], and multiphase [6], which is different from the typical crystallographic structure of the binary oxides for constituent elements. For example, formation of the amorphous structure was reported for $(\text{AlCrTaTiZr})\text{O}_x$ films grown at 350°C by direct current (DC) magnetron sputtering [7], while AlCrNbTaTi oxides with the same constituent elements, except for Zr being replaced by Nb, preferentially forms the rutile structure at

400°C [12]. In light of these features of AlCr-containing high-entropy oxide films, we strive to investigate the possibility of synthesizing corundum-structured (space group of $\text{R}\bar{3}\text{c}$) films.

There is a consensus that energetic irradiation from low-mass ions¹ is of importance for the phase formation and crystallinity of grown oxide thin films. Purely rutile structured TiO_2 film could be grown under intense bombardment from O^+ in contrast to the formation of the anatase phase under medium bombarding energy [13,14]. It was also demonstrated by Schneider et al. [15] that the crystallinity, as well as the crystal structure of Al_2O_3 films, are highly correlated to the ion energy of the irradiating Al^+ and O^+ ions. More importantly, in addition to the effect on the surface of the growing Al_2O_3 film, the increasing irradiation energy of Al^+ also show effect on the surface-adjacent layers. Thereby, subsurface processes such as phase transformation, defect generation and cluster dissociation are triggered, which opens for the growth of AlCr-containing multicomponent or high-entropy oxide films

* Corresponding author at: Plasma and Coatings Physics Division, Department of Physics, Chemistry, and Biology (IFM), Linköping University, Linköping SE-581 83, Sweden.

E-mail addresses: hdu3@gzu.edu.cn (H. Du), daniel.lundin@liu.se (D. Lundin).

¹ These ionic species are also classified as early-arriving ions in this study due to the early arrival time onto the substrate plane as compared to the high-mass ions sputtered from the same target

[16,17].

Inspired by these studies, energetic ion bombardment predominantly from early-arriving ions is in this study used to tune the growth of AlCr-containing multicomponent oxides. We investigate the effects on phase formation and nanoscale structural evolution in AlCrNbTi oxide films due to early-arriving ion irradiation. A HiPIMS discharge combined with a synchronized substrate acceleration pulse was used to provide acceleration for the positively charged ions. The constituent elements were selected based on our previous experience with the corresponding nitride system [18,19]. In sputtering processes, achieving the proper ion acceleration for dielectric films is challenging due to the acceleration voltage drop during film growth [20,21]. Therefore, this study employed a short (10 μ s) synchronized substrate bias at the end of the main HiPIMS pulse to minimize the film surface charging effect and accelerate the dominantly early-arriving ions.

The AlCrNbTi oxide films were grown using a 75-mm (3-inch) Al₂₅Cr₂₅Nb₂₅Ti₂₅ multicomponent target (99.95% purity, provided by Plansee AG) in an ultra-high vacuum system (VC1) with a base pressure of approximately 8×10^{-6} Pa. One-side polished silicon (001) wafers with dimensions of $10 \times 10 \times 0.5$ mm were used as substrates. The films were grown at 500°C in a working pressure of 0.4 Pa with a gas mixture of 26 sccm Ar and 2 sccm O₂. The target was powered by a HiPIMS unit (HIPSTER 1, Ionautics) and the substrate was biased by a 10 μ s-long synchronized pulse with a magnitude (U_{sync}) of -100, -200, -300, -400, and -500 V (see Fig. 1). A reference film grown by HiPIMS with a floating substrate potential (U_{float}) was also prepared. Measurements of the temporal evolution of the substrate ion current density (J_s) and ion fluxes were conducted in a separate high vacuum chamber (VC2) using a substrate current probe [20] and quadrupole mass spectrometer (PSM 003, Hidden analytical Ltd.), respectively. Elemental composition was determined using an energy-dispersive X-ray spectrometer (EDS, Oxford Instruments X-Max) in a scanning electron microscope (SEM, LEO Gemini 1550, Zeiss). Time-of-flight elastic recoil detection analysis (ToF-ERDA) was utilized for oxygen content measurement for the sample grown at $U_{\text{sync}} = -100$ V and the calibration of the rest of the samples. Crystallographic structures of the films were analyzed using X-ray diffraction (XRD) in a Bragg-Brentano (θ - 2θ) geometry on a high-resolution XRD diffractometer (PANalytical X'Pert PRO, Malvern Panalytical). X-ray pole figures were obtained on diffraction peaks $2\theta = 36.19^\circ$ and 63.73° using an x-ray diffractometer (PANalytical Empyrean diffractometer, Malvern Panalytical). Cross-sectional and plan-view images for the film grown at $U_{\text{sync}} = -500$ were captured using an (S)

TEM (FEI Tecnai G2 TF20 UT). (Detailed information for Experimental Details is referred to the Supplementary Material).

The temporal evolution of J_s is shown in Fig. 2(a). It is seen that the main portion of the ion flux arrives at the substrate after the end of the main HiPIMS pulse. Since J_s is proportional to the population of ions that reaches the film surface plane (if all ions are considered as singly charged), a small portion of the total ion flux, *i.e.*, the ion flux that reaches the substrate plane during τ_{sync} , is accelerated by the applied U_{sync} . To identify the ion species being accelerated by U_{sync} , the energy-integrated ion flux intensities (F_i) for both single- and double-charged ion fluxes are carried out and shown in Fig. 2(b) and (c), respectively. The evolution of F_i indicates that the arriving time of the species at the substrate position is highly dependent on the ion mass, *i.e.*, a similar peak position is observed from Ar⁺, Cr⁺, and Ti⁺ (see Fig. 2(b)), and Cr²⁺ and Ti²⁺ (see Fig. 2(c)). In addition, the arrival time for Ar²⁺ is earlier than the double-charged ion species which have similar ion masses. This phenomenon can be understood by the earlier ionization during the HiPIMS pulse [22] in combination with a shorter travel distance to the orifice of the mass spectrometer [23] of neutral Ar compared to the metal species from the target. From Fig. 2(a)–(c) (pink regions) we conclude that the 10 μ s-long substrate bias pulse only accelerates a fraction of the total impinging ion flux and that the accelerated fraction is predominantly composed of Al⁺, O⁺, Ar²⁺, and Al²⁺ ions. Note that the fraction of doubly charged Al²⁺ ions is assumed to be relatively low and sometimes not detectable by mass spectrometry due to a small cross section for electron impact ionization and short plasma transit time [24,25]. In our work, a weak signal from Al²⁺ is seen in Fig. 2(c), which is attributed to the high peak current density (~ 1.8 A/cm²). We here also show IEDFs for Al⁺ and Ar²⁺ ions (Fig. 2(d)). From this figure average primary kinetic energies of $E_0 \approx 15$ eV for Al⁺ and $E_0 \approx 10$ eV for Ar²⁺ are obtained.

The elemental composition of AlCrNbTi oxide films are shown in Table 1. The metallic elements in the film differ from the near-equal atomic fractions, with a substantially higher-than-nominal Al content, and correspondingly somewhat lower Ti content. The cation/anion ratio in the film, in a range of 1.68/3 - 1.76/3, is slightly lower than the ratio of 2/3 for a stoichiometric Al₂O₃ and Cr₂O₃ compound showing excessive amount of oxygen in the film (see Table 1).

The XRD patterns of the AlCrNbTi oxide films grown at different U_{sync} are shown in Fig. 3(a). Peaks are observed at 2θ locations in the range of $35.7 - 36.4^\circ$ and $63.7 - 65.3^\circ$ (dependent on U_{sync}), which are close to the 110 and 214 (or 300) reflections of the α crystal structure (space group R $\bar{3}c$ / 167), corresponding to Cr₂O₃ (eskolait, ICDD PDF 00-038-1479) or Al₂O₃ (corundum, ICDD PDF 00-046-1212). Due to the overlap between the 214 and 300 reflections for solid solution corundum (Cr,Al)₂O₃ [26], x-ray pole figures were measured to further investigate the growth direction (Fig. 3(b)). In the pole figure acquired at the $2\theta = 63.73^\circ$ reflection, diffraction is only detected at the center ($\psi = 0^\circ$) of the pole figure. For the pole figure with $2\theta = 36.19^\circ$, a ring appears at $\psi \approx 30^\circ$. The unstrained angles between (110) and (214) planes in eskolait-Cr₂O₃ and corundum-Al₂O₃ are 27.6° and 27.7° , respectively, and the unstrained angles between (110) and (300) are 30° for both of the phases (from the lattice parameters given in ICDD PDF 00-038-1479 and ICDD PDF 00-046-1212). Therefore, the observed ψ angle confirms a corundum crystal structure, and the reflections at $2\theta = 36.19^\circ$ and 63.73° corresponds to the (110) and (300) planes, respectively. The peak positions, however, shift to lower angles as compared to unstrained peak positions for corundum-Al₂O₃, *i.e.*, $2\theta = 37.78^\circ$ for (110) and 68.22° for (300), as well as $2\theta = 36.20^\circ$ for (110) and 65.11° for (300) of eskolait-Cr₂O₃. This observation can be understood by the peak shift of corundum-structured multicomponent oxides, for example $2\theta = 36.72^\circ$ for (110) and 66.13° for (300) of α -(Al_{0.75}Cr_{0.22}Ti_{0.03})₂O₃, where the identical peak positions for this compound also shifts to lower angles as compared with corundum-Al₂O₃ due to the increased lattice constant [27]. For the films grown with U_{float} and $U_{\text{sync}} = -100$ V, low

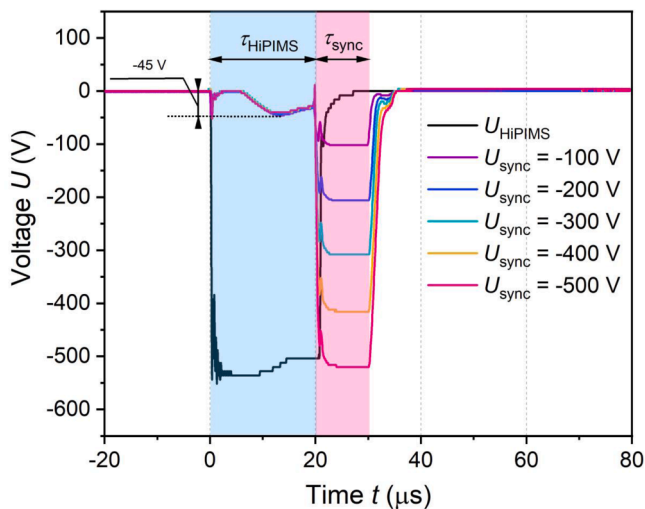


Fig. 1. Target voltage (U_{HiPIMS}) and synchronized substrate voltage (U_{sync}) waveforms. The pulse length of the main HiPIMS pulse and the synchronized substrate bias are marked as τ_{HiPIMS} and τ_{sync} , respectively.

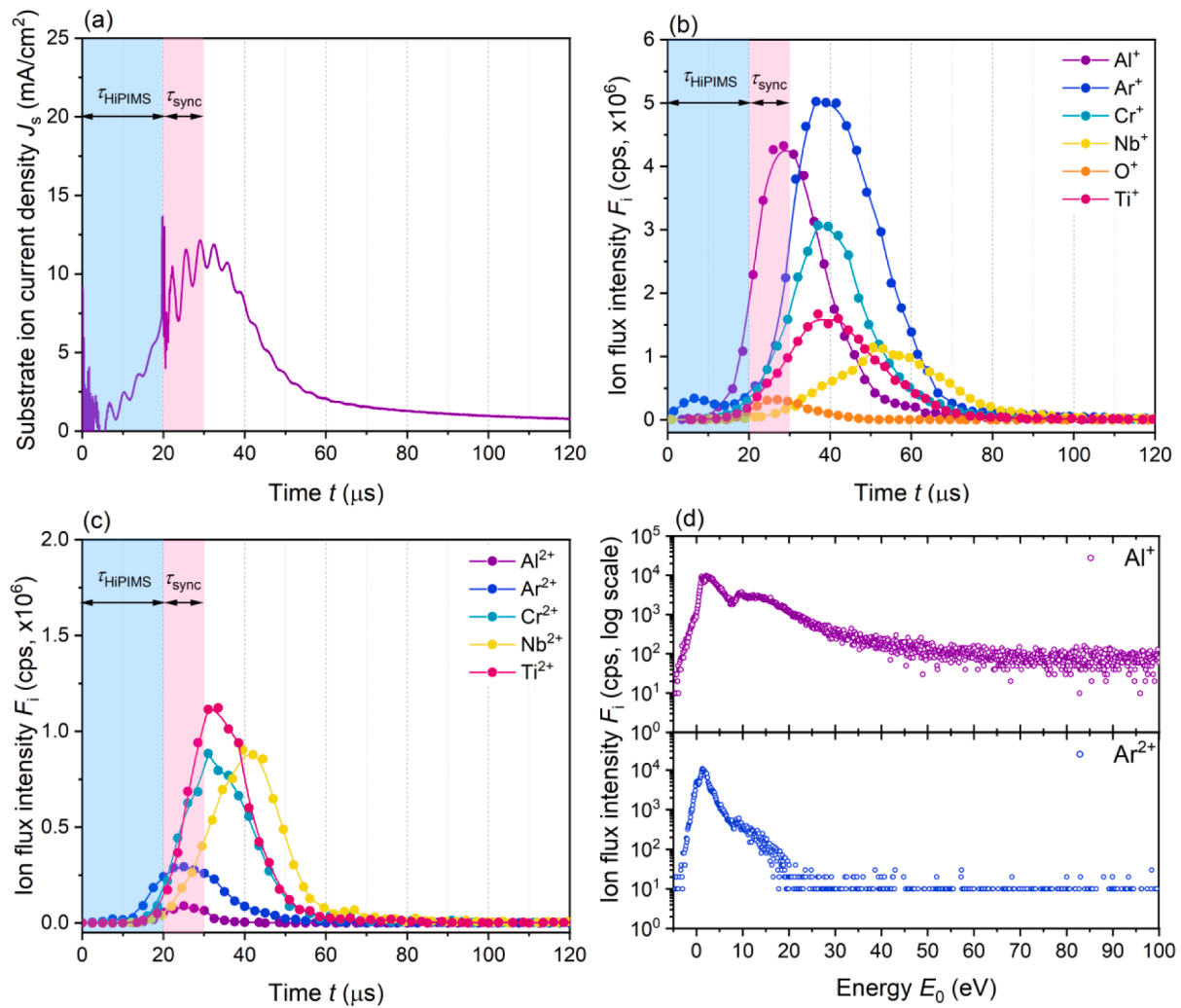


Fig. 2. Temporal evolution of (a) the substrate ion current density J_s , (b) the energy-integrated ion flux intensities F_i of single-charged Al^+ (27 amu), Ar^+ (40 amu), Cr^+ (52 amu), Nb^+ (93 amu), O^+ (16 amu), and Ti^+ (48 amu) ions, and (c) the energy-integrated ion flux intensities F_i of double-charged Al^{2+} (27 amu), Ar^{2+} (40 amu), Cr^{2+} (52 amu), Nb^{2+} (93 amu), and Ti^{2+} (48 amu) ions. (d) Time-averaged IEDFs of Al^+ and Ar^{2+} ions (IEDFs for O^+ are not shown due to the low intensity). The pulse length of the main HiPIMS pulse and the synchronized substrate bias is marked as τ_{HiPIMS} and τ_{sync} , respectively.

Table 1

Elemental composition and cation/anion ratio for AlCrNbTi oxide films. The elemental compositions of the as-deposited films are measured by EDS and calibrated by using the oxygen content of the sample grown at $U_{\text{sync}} = -100$ V as determined by ToF-ERDA. The oxygen concentration is normalized to 3 and the following concentration for the metallic element is calculated by using the cation/anion ratio determined by film composition.

U_{sync}	Atomic composition (± 0.5 at.% estimated)					Normalized stoichiometry	
	O	Ti	Nb	Cr	Al	Metallic element	Oxygen
floating	64.1	6.7	9.0	8.7	11.4	1.68	3
-100	64.1	6.9	8.7	8.7	11.5	1.68	3
-200	63.5	7.0	8.6	9.0	11.8	1.72	3
-300	63.8	7.1	8.4	9.2	11.5	1.70	3
-400	63.4	7.0	8.4	9.6	11.6	1.73	3
-500	63.0	7.4	8.6	9.8	11.3	1.76	3

peak intensities corresponding to the growth of (110) and (300) planes is seen, revealing low film crystallinity. In contrast, as U_{sync} increases, film growth transforms from the (110) to the (300) plane, and the absolute intensity of the 300 peak increases with increasing U_{sync} . It is also seen that the position of the 300 peak shifts towards lower angles as U_{sync}

increases, indicating an expansion of the out-of-plane lattice. A possible explanation for this phenomenon is related to an increasing defect number density within grains induced by the elevated ion irradiation energy [28,29]. In general, it can be concluded that the increasing ion irradiation energy significantly increases film crystallinity and influences the preferred orientation of the film, i.e., the growth towards the low-energy (300) plane during high-energy ion irradiation, which is consistent with studies of $\alpha\text{-Cr}_2\text{O}_3$ and $\alpha\text{-Al}_2\text{O}_3$ [30–32].

A low magnification cross-sectional STEM image of AlCrNbTi oxide films grown at $U_{\text{sync}} = -500$ V is shown in Fig. 4(a). The film exhibits a columnar structure. The corresponding EDS elemental maps, shown in Fig. 4(b), were collected from the boxed region b in Fig. 4(a), and show a homogenous film. The selected area electron diffraction (SAED) pattern in Fig. 4(c) acquired close to the surface of the film is attributed to the corundum (R3c) structure. Fig. 4(d) shows the high-resolution TEM image. The corresponding Fast Fourier Transformation (FFT) pattern (Fig. 4(e)) closely matches the simulated diffraction from $\alpha\text{-Al}_2\text{O}_3$ viewed along the [001] direction (Fig. 4(f)). Thus, we here can conclude that the crystalline $\alpha\text{-Al}_2\text{O}_3$ type corundum phase is obtained at $U_{\text{sync}} = -500$ V. As seen both in the plan-view TEM image in Fig. 4(g) and the additional spots in the SAED pattern (Fig. 4(c)), high-number-density stacking faults are identified in individual film grains, which can be simultaneously confirmed by the high-resolution TEM images (Fig. 4(h))

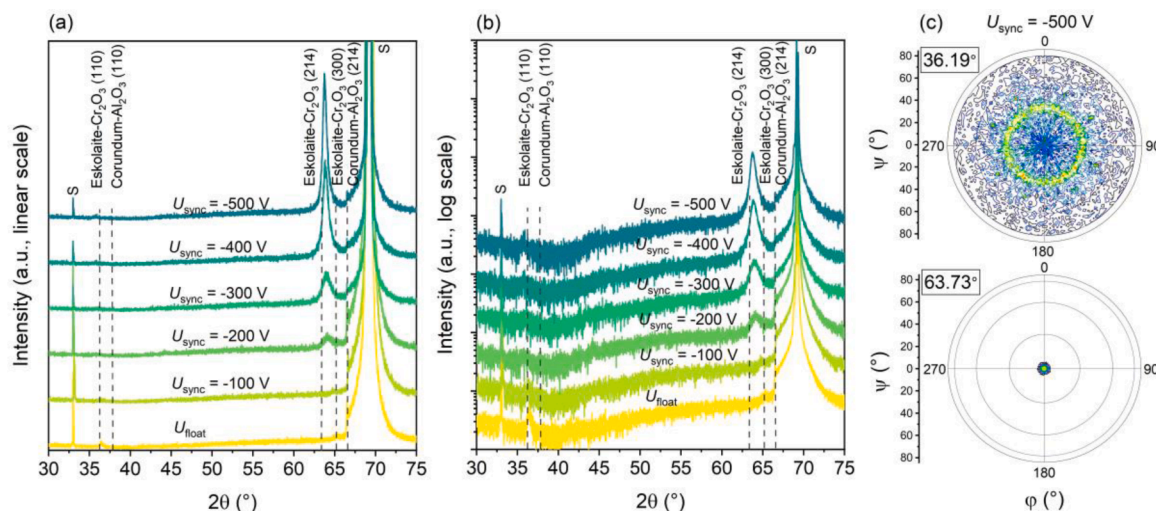


Fig. 3. θ - 2θ X-ray diffractograms of AlCrNbTi oxide films grown with the floating substrate bias (U_{float}) and synchronized substrate bias (U_{sync}) of -100, -200, -300, -400, and -500 V in (a) linear scale and (b) log scale. The dot vertical lines belong to the unstrained peaks of eskolaite-type Cr_2O_3 (ICDD PDF 00-038-1479) and corundum-type Al_2O_3 (ICDD PDF 00-046-1212). (c) X-ray pole figures are taken from the 110 peak at $2\theta = 36.19^\circ$ and 300 peak at $2\theta = 63.73^\circ$, respectively. Note that the 2θ range of 30° – 75° is shown in (a) and (b) since no peaks were detected at $2\theta = 20^\circ$ – 30° .

and the corresponding FFT patterns (Fig. 4(i) and (j)). The FFT patterned from a single grain is shown in Fig. 4(j). Indexing this pattern is complicated by the presence of stacking fault defects, resulting in the presence of additional spots. A close match, however, is found to the pattern obtained along the $[1\bar{1}0]$ direction. The FFT from several adjacent grains show well-defined geometric patterns. This indicates that in the in-plane orientation the grains are not randomly orientated, but rather have preferred orientations. The strengthening benefits from stacking faults or nanotwinned structures are assumed to overcome the hardness-toughness trade-off for materials [33,34]. The elevated ion irradiation energy shows that it is indeed possible to overcome the extremely high stacking fault formation threshold of oxides, e.g., the stacking fault energy in α - Al_2O_3 is 1.2–4.6 J/m² for $\{0001\}$ planes and 0.3–0.9 J/m² for $\{10\bar{1}0\}$ and $\{11\bar{2}0\}$ planes [35]. Our results open up for new processes for ceramic film deposition, as stacking faults are precursors for nanotwin structures [36].

We are interested in whether we can draw conclusions on the effects of ion irradiation on defects and phase transformation in early-arriving ions. During ion-assisted film growth, the film structure can be rearranged due to thermal spikes created by the irradiating ions [37]. This can induce thermal hopping inside the expanding heat pulses and result in surface diffusion, local heating, and recrystallization, leading to film densification and changes in growth, such as preferred orientation and crystallite size [38]. Note that a thermal spike-induced temperature increase predominantly depends on the surface migration energy, rather than the ion flux density and ion energy [39]. As a result, low-energy ions tend to induce thermal spikes leading to higher adatom mobility and the growth of grains with the lowest surface energy planes. Differently, the high-energy ions penetrate grains and generate defects according to the channeling-related mechanism, and thereby induce a film growth towards more open-channeling planes [39]. Due to the high energy and low mass of the irradiating ions in this study, we do not expect a predominately thermal spike effect, but instead, the channeling effect is assumed to be more important. As the TiAlCrNb oxide film grown at the floating potential prefer to grow in an amorphous structure, the high-energy irradiation from low-mass ions drives the film towards a state of minimum volume free-energy density, with major crystallographic channeling directions aligned parallel to the incident ion direction. For crystals with an hcp structure, the strongest channeling direction corresponds to $\langle 2\bar{1}\bar{1}0 \rangle$ directions, perpendicular to the $(30\bar{3}0)$ plane [40]. Therefore, high-energy ion irradiation promotes both

higher crystallinity and growth of TiAlCrNb oxide film towards the more open-channeling (300), i.e., $(30\bar{3}0)$, plane (see Fig. 3), i.e., different from preferred $(10\bar{1}4)$ orientation [41,42]. Due to the fiber texture feature of the grown TiAlCrNb oxide films (see Fig. 3(c)), defects such as stacking faults and nanowins can be generated in grains with out-of-plane growth directions not parallel to the channeling direction (see Fig. 4). The fraction of ions incident parallel to channeling directions and subsequently channeled increases with increasing ion energy and/or decreasing ion mass [39], giving rise to the increasing (300) peak intensities with increasing U_{sync} in the present work (see Fig. 3).

The remaining question is whether the formation of the α -phase in TiAlCrNb oxide is related to its constituent elements. It has been suggested that the incorporation of elements such as Cr and Fe can lower the growth temperature of α - Al_2O_3 . For example, a corundum-structured Al-Cr-Fe-O film can be grown using cathodic arc evaporation at a deposition temperature of 550°C [42,43]. It has also been found that the growth of the corundum phase at a lower deposition temperature (500°C) can be achieved at relatively high oxygen partial pressure using a $Cr_{0.3}Al_{0.7}$ target [44]. In general, the mechanism of low-temperature synthesis of high-temperature phases with the assistance of a dopant lies in the lower formation temperature of α - Cr_2O_3 and α - Fe_2O_3 , which stabilizes the formation of α - Al_2O_3 in the same space group at low temperature. However, for the TiAlCrNb oxide investigated in this study, there is no clear indication of corundum forming at the growth temperature of 500°C. It has been shown that $(AlCrTaTiZr)O_x$ [7] and AlCrNbTaTi oxide [12] prefer to grow in amorphous and rutile structures, respectively, at 350–400°C, accompanied by low ion acceleration conditions. Furthermore, the formation of a cubic structure of $Al_xCoCrCuFeNi$ oxide [11] as well as $(Al_{0.31}Cr_{0.20}Fe_{0.14}Ni_{0.35})O$ [45] films and an amorphous $(TiAlCrZr)O$ film [46], are suggested, where more elements are able to form Me_2O_3 -type oxides at low temperature with the $R\bar{3}c$ space group. In particular, the $Al_xCoCrCuFeNi$ oxide shows no phase transformation even after being annealed at 500°C for 5 h [11]. Therefore, we speculate that the formation of the here-observed corundum structure of TiAlCrNb oxide mainly stem from the increasing energy of ion irradiation.

In conclusion, this study clearly demonstrates that increasing ion irradiation energy from early-arriving ions at a constant growth temperature results in the elevated crystallinity and the formation of a single-phase corundum structure at the expense of the amorphous matrix. Additionally, the study discovered the generation of high-density

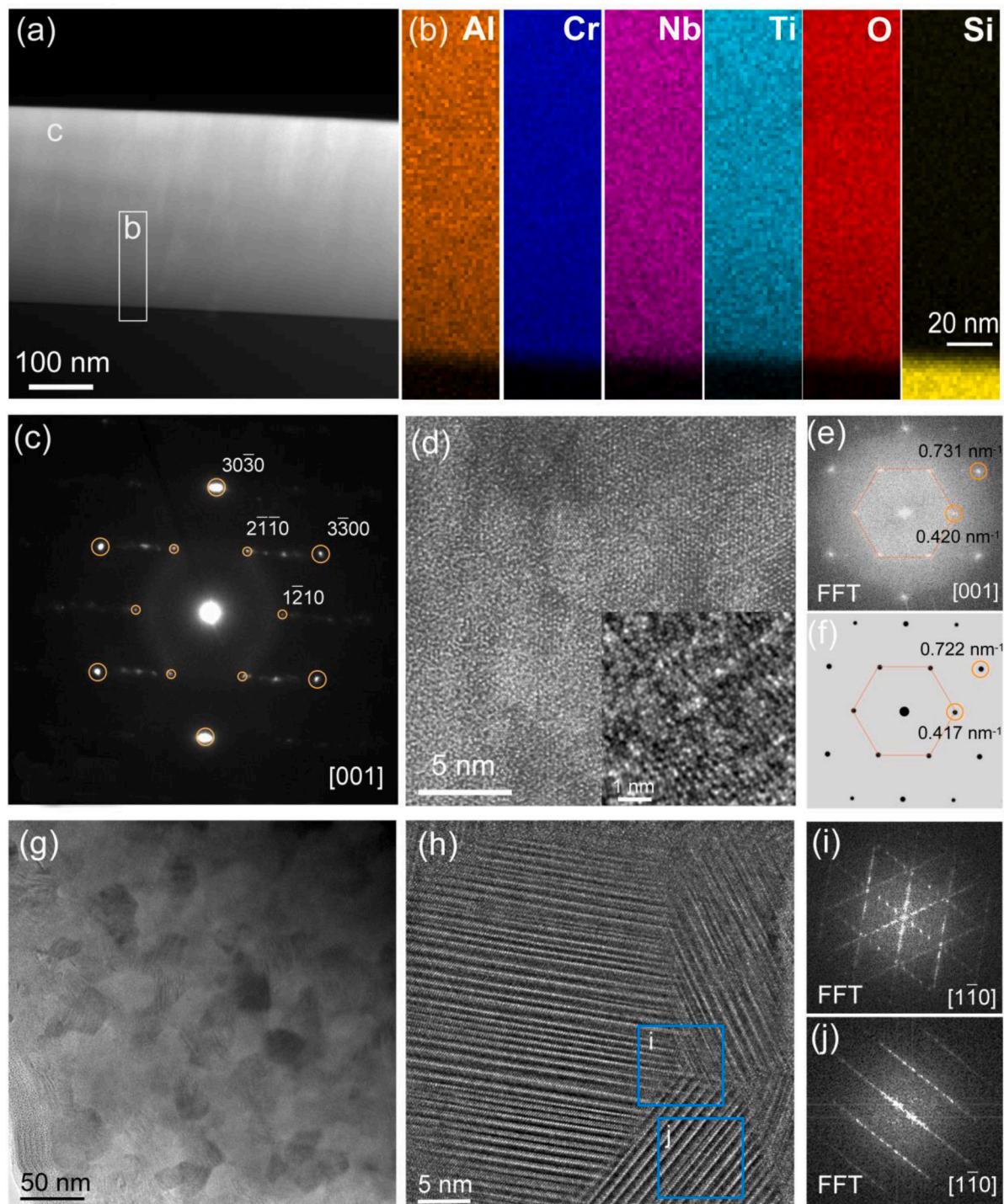


Fig. 4. (a) Cross-sectional low-resolution STEM image of AlCrNbTi oxide films grown at $U_{\text{sync}} = -500$ V. (b) EDS mapping acquired from region b in (a) for Al, Cr, Nb, Ti, O, and Si. (c) the SAED pattern is taken from the top area c of the film in (a). (d) High-resolution TEM image of AlCrNbTi oxide films grown at $U_{\text{sync}} = -500$ V and its magnified image (bottom right). (e) Fast Fourier Transformation (FFT) pattern of (d), in comparison with (f) the simulated diffraction on $\alpha\text{-Al}_2\text{O}_3$ viewed in the [001] direction. (g) low-resolution and (h) high-resolution plan-view STEM images of AlCrNbTi oxide films grown at $U_{\text{sync}} = -500$ V. (i) and (j) are FFT patterns at area i and j in (h), respectively.

stacking faults (or nanotwin) structure in the $U_{\text{sync}} = -500$ V film. These findings hold great potential for growing crystalline high-temperature phases and for tuning the nanoscale structure of oxide films using energetic ion irradiation, with the possibility of applications in hard-coating and dielectric fields.

CRediT authorship contribution statement

Hao Du: Conceptualization, Investigation, Data curation, Formal analysis, Writing – original draft, Funding acquisition. **Rui Shu:** Investigation, Data curation, Formal analysis, Writing – review & editing. **Robert Boyd:** Investigation, Data curation, Formal analysis, Writing – review & editing. **Arnaud le Febvrier:** Investigation, Formal analysis, Writing – review & editing. **Mauricio A. Sortica:** Data curation, Formal

analysis, Writing – review & editing. **Daniel Primetzhofer**: Project administration, Data curation, Formal analysis, Writing – review & editing. **Ulf Helmersson**: Project administration, Conceptualization, Supervision, Writing – review & editing, Funding acquisition. **Per Eklund**: Project administration, Conceptualization, Supervision, Writing – review & editing, Funding acquisition. **Daniel Lundin**: Project administration, Conceptualization, Supervision, Writing – review & editing, Funding acquisition.

Declaration of Competing Interest

The authors declare no competing interests.

Acknowledgments

The work was supported financially by the VINNOVA Competence Centre FunMat-II (grant no. 2016-05156), the Swedish Government Strategic Research Area in Materials Science on Functional Materials at Linköping University (Faculty Grant SFO-Mat-LiU No. 2009 00971), the Knut and Alice Wallenberg Foundation through the Wallenberg Academy Fellows program (KAW-2020.0196), the Swedish Research Council (Grant No. VR 2021-03826). D.L. acknowledges the Swedish Research Council (Grant No. VR 2018-04139) and the Eurostars program (Grant No. E!114277, IonDrive). H. D. acknowledges the financial support from the National Natural Science Foundation of China (Grant No. 52165021, 51805102) and the Science and Technology Foundation of Guizhou Province (Grant No. [2020]1Y228). Accelerator operation was supported by Swedish Research Council VR-RFI (Contract No. 2019-00191) and the Swedish Foundation for Strategic Research (Contract No. RIF14-0053). H. D. is grateful for the backing of the State Key Laboratory of Public Big Data, Guizhou University.

Data availability

The data that support these findings are available from the corresponding author on request.

Supplementary materials

Supplementary material associated with this article can be found, in the online version, at [doi:10.1016/j.scriptamat.2023.115578](https://doi.org/10.1016/j.scriptamat.2023.115578).

References

- [1] C.M. Rost, E. Sachet, T. Borman, A. Moballegh, E.C. Dickey, D. Hou, J.L. Jones, S. Curtarolo, J.-P. Maria, Entropy-stabilized oxides, *Nat Commun.* 6 (2015) 8485, <https://doi.org/10.1038/ncomms9485>.
- [2] C. Oses, C. Toher, S. Curtarolo, High-entropy ceramics, *Nat Rev. Mater.* 5 (2020) 295–309, <https://doi.org/10.1038/s41578-019-0170-8>.
- [3] D.B. Miracle, O.N. Senkov, A critical review of high entropy alloys and related concepts, *Acta Mater.* 122 (2017) 448–511, <https://doi.org/10.1016/j.actamat.2016.08.081>.
- [4] Z. Liu, P. Huang, L. Sun, Y. Liu, J. Qu, J. Cairney, Z. Zheng, Z.M. Wang, N.A. Khan, Z. Lai, L. Fu, B. Teng, C. Zhou, H. Zhao, F. Xu, P. Xiong, J. Zhu, P. Yuan, K. Tsoutas, B. Akhavan, M.M. Bilek, S.P. Ringer, K.S. Novoselov, Self-repairing high entropy oxides, *ArXiv:2112.11747 [Cond-Mat]*, <http://arxiv.org/abs/2112.11747>.
- [5] A. Mao, H.-Z. Xiang, Z.-G. Zhang, K. Kuramoto, H. Zhang, Y. Jia, A new class of spinel high-entropy oxides with controllable magnetic properties, *J. Mag. Mater.* 497 (2020), 165884, <https://doi.org/10.1016/j.jmmm.2019.165884>.
- [6] M.S. Lal, R. Sundara, High entropy oxides—a cost-effective catalyst for the growth of high yield carbon nanotubes and their energy applications, *ACS Appl. Mater. Interfaces* (2019), <https://doi.org/10.1021/acsami.9b08794>.
- [7] M.-I. Lin, M.-H. Tsai, W.-J. Shen, J.-W. Yeh, Evolution of structure and properties of multi-component (AlCrTaTiZr)Ox films, *Thin Solid Films* 518 (2010) 2732–2737, <https://doi.org/10.1016/j.tsf.2009.10.142>.
- [8] N. Behravan, A. Farhadzadeh, S. Ghasemi, A. Khademi, H. Shojaei, H. Ghomi, The pressure dependence of structure and composition of sputtered AlCrSiTiMoO high entropy thin film, *J. Alloys Comp.* 852 (2021), 156421, <https://doi.org/10.1016/j.jallcom.2020.156421>.
- [9] N.A. Khan, B. Akhavan, Z. Zheng, H. Liu, C. Zhou, H. Zhou, L. Chang, Y. Wang, Y. Liu, L. Sun, Marcela.M. Bilek, Z. Liu, Nanostructured AlCoCrCu0.5FeNi high entropy oxide (HEO) thin films fabricated using reactive magnetron sputtering, *Appl. Surface Sci.* 553 (2021), 149491, <https://doi.org/10.1016/j.apsusc.2021.149491>.
- [10] T.-K. Chen, M.-S. Wong, Structure and properties of reactively-sputtered AlxCoCrCuFeNi oxide films, *Thin Solid Films* 516 (2007) 141–146, <https://doi.org/10.1016/j.tsf.2007.06.142>.
- [11] T.-K. Chen, M.-S. Wong, Thermal stability of hard transparent AlxCoCrCuFeNi oxide thin films, *Surface Coatings Technol.* 203 (2008) 495–500, <https://doi.org/10.1016/j.surfcoat.2008.05.023>.
- [12] A. Kirmbaurer, C. Spadt, C.M. Koller, S. Kolozsvári, P.H. Mayrhofer, High-entropy oxide thin films based on Al–Cr–Nb–Ta–Ti, *Vacuum* 168 (2019), 108850, <https://doi.org/10.1016/j.vacuum.2019.108850>.
- [13] A. Amin, D. Köhl, M. Wuttig, The role of energetic ion bombardment during growth of TiO₂ thin films by reactive sputtering, *J. Phys. D Appl. Phys.* 43 (2010), 405303, <https://doi.org/10.1088/0022-3727/43/40/405303>.
- [14] F. Cemin, M. Tsukamoto, J. Keraudy, V.G. Antunes, U. Helmersson, F. Alvarez, T. Minea, D. Lundin, Low-energy ion irradiation in HiPIMS to enable anatase TiO₂ selective growth, *J. Phys. D: Appl. Phys.* 51 (2018), 235301, <https://doi.org/10.1088/1361-6463/aac080>.
- [15] J.M. Schneider, W.D. Sproul, A. Matthews, Reactive ionized magnetron sputtering of crystalline alumina coatings, *Surface Coatings Technol.* 98 (1998) 1473–1476, [https://doi.org/10.1016/S0257-8972\(97\)00140-0](https://doi.org/10.1016/S0257-8972(97)00140-0).
- [16] K. Sarakinos, D. Music, F. Nahif, K. Jiang, A. Braun, C. Zilkens, J.M. Schneider, Ionized physical vapor deposited Al₂O₃ films: does subplantation favor formation of α -Al₂O₃? *Phys. Status Solidi (RRL) – Rap. Res. Lett.* 4 (2010) 154–156, <https://doi.org/10.1002/pssr.201004133>.
- [17] D. Music, F. Nahif, K. Sarakinos, N. Friederichsen, J.M. Schneider, Ab initio molecular dynamics of Al irradiation-induced processes during Al₂O₃ growth, *Appl. Phys. Lett.* 98 (2011), 111908, <https://doi.org/10.1063/1.3570650>.
- [18] R. Shu, H. Du, G. Sadowski, M.M. Dorri, J. Rosen, M.A. Sortica, D. Primetzhofer, D. Lundin, A. le Febvrier, P. Eklund, Multicomponent Ti_xNb_yCrAl nitride films deposited by dc and high-power impulse magnetron sputtering, *Surface Coat. Technol.* 426 (2021), 127743, <https://doi.org/10.1016/j.surfcoat.2021.127743>.
- [19] H. Du, R. Shu, R. Boyd, A. le Febvrier, U. Helmersson, P. Eklund, D. Lundin, Evolution of microstructure and properties of Ti_xNb_yCrAlHfN films grown by unipolar and bipolar high-power impulse magnetron co-sputtering: the role of growth temperature and ion bombardment, *Surface Coat. Technol.* 459 (2023), 129389, <https://doi.org/10.1016/j.surfcoat.2023.129389>.
- [20] H. Du, M. Zanaška, N. Brenning, U. Helmersson, Bipolar HiPIMS: the role of capacitive coupling in achieving ion bombardment during growth of dielectric thin films, *Surface Coat. Technol.* 416 (2021), 127152, <https://doi.org/10.1016/j.surfcoat.2021.127152>.
- [21] H. Du, M. Zanaška, U. Helmersson, D. Lundin, On selective ion acceleration in bipolar HiPIMS: a case study of (Al,Cr)₂O₃ film growth, *Surface Coat. Technol.* 454 (2023), 129153, <https://doi.org/10.1016/j.surfcoat.2022.129153>.
- [22] C. Vitellari, D. Lundin, G.D. Stancu, N. Brenning, J. Bretagne, T. Minea, Argon metastables in HiPIMS: time-resolved tunable diode-laser diagnostics, *Plasma Sources Sci. Technol.* 21 (2012), 025010, <https://doi.org/10.1088/0963-0252/21/2/025010>.
- [23] N. Britun, S. Konstantinidis, R. Snyders, An overview on time-resolved optical analysis of HiPIMS discharge, *Plasma Processes Polymers* 12 (2015) 1010–1027, <https://doi.org/10.1002/ppap.201500051>.
- [24] C. Huo, D. Lundin, J.T. Gudmundsson, M.A. Raadu, J.W. Bradley, N. Brenning, Particle-balance models for pulsed sputtering magnetrons, *J. Phys. D Appl. Phys.* 50 (2017), 354003, <https://doi.org/10.1088/1361-6463/aa7d35>.
- [25] G. Greczynski, J. Lu, J. Jensen, S. Bolz, W. Kölker, Ch. Schiffrs, O. Lemmer, J. E. Greene, L. Hultman, A review of metal-ion-flux-controlled growth of metastable TiAlN by HIPIMS/DCMS co-sputtering, *Surface Coat. Technol.* 257 (2014) 15–25, <https://doi.org/10.1016/j.surfcoat.2014.01.055>.
- [26] K. Pedersen, J. Böttiger, M. Sridharan, M. Sillassen, P. Eklund, Texture and microstructure of Cr₂O₃ and (Cr,Al)₂O₃ thin films deposited by reactive inductively coupled plasma magnetron sputtering, *Thin Solid Films* 518 (2010) 4294–4298, <https://doi.org/10.1016/j.tsf.2010.01.008>.
- [27] H. Liu, H. Du, G. Xian, Y. Chen, H. Dai, Ab-initio calculations of corundum structured α -(Al_{0.75}Cr_{0.22}Me_{0.03})₂O₃ compounds (Me = Si, Fe, Mn, Ti, V and Y), *Comput. Mater. Sci.* 212 (2022), 111601, <https://doi.org/10.1016/j.commatsci.2022.111601>.
- [28] I. Petrov, L. Hultman, J.-E. Sundgren, J.E. Greene, Polycrystalline TiN films deposited by reactive bias magnetron sputtering: effects of ion bombardment on resputtering rates, film composition, and microstructure, *J. Vacuum Sci. Technol. Vacuum Surfaces Films* 10 (1992) 265–272, <https://doi.org/10.1116/1.578074>.
- [29] F. Adibi, I. Petrov, J.E. Greene, L. Hultman, J.-E. Sundgren, Effects of high-flux low-energy (20–100 eV) ion irradiation during deposition on the microstructure and preferred orientation of Ti 0.5 Al 0.5 N alloys grown by ultra-high-vacuum reactive magnetron sputtering, *J. Appl. Phys.* 73 (1993) 8580–8589, <https://doi.org/10.1063/1.353388>.
- [30] J. Sun, T. Stirner, A. Matthews, Molecular dynamics simulation of the (0001) α -Al₂O₃ and α -Cr₂O₃ surfaces, *Surface Sci.* 601 (2007) 1358–1364, <https://doi.org/10.1016/j.susc.2006.12.091>.
- [31] J. Sun, T. Stirner, A. Matthews, Structure and surface energy of low-index surfaces of stoichiometric α -Al₂O₃ and α -Cr₂O₃, *Surface Coat. Technol.* 201 (2006) 4205–4208, <https://doi.org/10.1016/j.surfcoat.2006.08.061>.
- [32] P. Eklund, M. Sridharan, M. Sillassen, J. Böttiger, α -Cr₂O₃ template-texture effect on α -Al₂O₃ thin-film growth, *Thin Solid Films* 516 (2008) 7447–7450, <https://doi.org/10.1016/j.tsf.2008.03.038>.

- [33] K. Lu, L. Lu, S. Suresh, Strengthening materials by engineering coherent internal boundaries at the nanoscale, *Science* 324 (2009) 349–352, <https://doi.org/10.1126/science.1159610>.
- [34] Y. Wei, Y. Li, L. Zhu, Y. Liu, X. Lei, G. Wang, Y. Wu, Z. Mi, J. Liu, H. Wang, H. Gao, Evading the strength–ductility trade-off dilemma in steel through gradient hierarchical nanotwins, *Nat Commun.* 5 (2014) 3580, <https://doi.org/10.1038/ncomms4580>.
- [35] P.R. Kenway, Calculated stacking-fault energies in α -Al₂O₃, *Philosoph. Mag.* B 68 (1993) 171–183, <https://doi.org/10.1080/01418639308226398>.
- [36] L. Sun, X. He, J. Lu, Nanotwinned and hierarchical nanotwinned metals: a review of experimental, computational and theoretical efforts, *Npj Comput. Mater.* 4 (2018) 6, <https://doi.org/10.1038/s41524-018-0062-2>.
- [37] K. Müller, Monte Carlo calculation for structural modifications in ion-assisted thin film deposition due to thermal spikes, *J. Vacuum Sci. Technol. A* 4 (1986) 184–188, <https://doi.org/10.1116/1.573468>.
- [38] K.-H. Müller, Ion-beam-induced epitaxial vapor-phase growth: a molecular-dynamics study, *Phys. Rev. B* 35 (1987) 7906–7913, <https://doi.org/10.1103/PhysRevB.35.7906>.
- [39] G. Carter, Influence of thermal spikes on preferred grain orientation in ion-assisted deposition, *Phys. Rev. B* 62 (2000) 8376–8390, <https://doi.org/10.1103/PhysRevB.62.8376>.
- [40] K. Nordlund, F. Djurabekova, G. Hobler, Large fraction of crystal directions leads to ion channeling, *Phys. Rev. B* 94 (2016), 214109, <https://doi.org/10.1103/PhysRevB.94.214109>.
- [41] E. Wallin, T.I. Selinder, M. Elfving, U. Helmersson, Synthesis of α -Al₂O₃ thin films using reactive high-power impulse magnetron sputtering, *EPL* 82 (2008) 36002, <https://doi.org/10.1209/0295-5075/82/36002>.
- [42] C.M. Koller, J. Ramm, S. Kolozsvári, F. Munnik, J. Paulitsch, P.H. Mayrhofer, Corundum-type Fe-doped cathodic arc evaporated Al–Cr–O coatings, *Scripta Mater.* 97 (2015) 49–52, <https://doi.org/10.1016/j.scriptamat.2014.10.037>.
- [43] C.M. Koller, S.A. Glatz, S. Kolozsvári, J. Ramm, P.H. Mayrhofer, Influence of substrate bias on structure and mechanical properties of arc evaporated (Al,Cr)2O₃ and (Al,Cr,Fe)2O₃ coatings, *Surface Coat. Technol.* 319 (2017) 386–393, <https://doi.org/10.1016/j.surfcoat.2017.04.023>.
- [44] Z.R. Liu, X. Sun, J.W. Du, L. Chen, Enhanced crystallization of α -(Cr, Al)2O₃ coatings with increasing oxygen pressure, *Surface Coat. Technol.* 445 (2022), 128705, <https://doi.org/10.1016/j.surfcoat.2022.128705>.
- [45] Z.-M. Yang, K. Zhang, N. Qiu, H.-B. Zhang, Y. Wang, J. Chen, Effects of helium implantation on mechanical properties of (Al_{0.31}Cr_{0.20}Fe_{0.14}Ni_{0.35})O high entropy oxide films*, *Chinese Phys. B* 28 (2019), 046201, <https://doi.org/10.1088/1674-1056/28/4/046201>.
- [46] L. Hu, F. Zhong, J. Zhang, S. Zhao, Y. Wang, G. Cai, T. Cheng, G. Wei, S. Jia, D. Zhang, R. Yin, Z. Chen, C. Jiang, F. Ren, High hydrogen isotopes permeation resistance in (TiVAlCrZr)O multi-component metal oxide glass coating, *Acta Mater.* 238 (2022), 118204, <https://doi.org/10.1016/j.actamat.2022.118204>.